



AIAA-95-0469

**Simulation of Transient Hypersonic Flow
Using the ENO Schemes**

C. Chiu and X. Zhong
University of California, Los Angeles
Los Angeles, CA

**33rd Aerospace Sciences
Meeting and Exhibit
January 9-12, 1995 / Reno, NV**

SIMULATION OF TRANSIENT HYPERSONIC FLOW USING THE ENO SCHEMES

Chien-Erh Chiu * and Xiaolin Zhong †

Mechanical, Aerospace and Nuclear Engineering Department
University of California, Los Angeles, CA 90095

Abstract

This paper is concerned with direct numerical simulation of two-dimensional transient hypersonic flow using the essentially non-oscillatory (ENO) schemes for the Euler and Navier-Stokes equations. The ENO schemes are used because their shock capturing capability and uniform high-order accuracy away from the shock waves are particularly suitable for transient hypersonic flow calculations. The accuracy of the ENO schemes are numerically tested by applying them to linear viscous model equations and the Navier-Stokes equations. Two applications are considered for unsteady hypersonic flow simulation. The first application is a shock-shock interference heating problem. The unsteady mechanism of type IV shock interference flow is numerically investigated through test cases of different Reynolds numbers. The results show that the inherent unsteadiness of interference flow is dominated by the viscous interactions at high Reynolds numbers. The second application is the interaction of a planar acoustic wave with a bow shock in hypersonic flow over a cylinder. Numerical results are compared with simple analytical solutions. The results show that the disturbances are greatly amplified near the stagnation point, which demonstrates the importance of including the bow shock in the direct numerical simulations of the receptivity of hypersonic boundary layer to free stream disturbances.

Introduction

The unsteadiness of hypersonic flow plays an important role in many viscous hypersonic flow fields that are important for developing future hypersonic vehicles. Two hypersonic flow problems involving unsteadiness of the flow are studied in this paper.

The first flow problem is the shock-shock interference heating flow created by the interaction of an impinging shock and a bow shock wave on the cowl-lip surface of a hypersonic inlet^[1]. The interference heating problem is a crucial problem in designing hypersonic vehicles because the heating rates generated on the surface

can be an order of magnitude higher than those without the interaction with the impinging shock. Among the six types of shock interference patterns classified by Edney^[2], type IV interference occurs when the impinging shock intersects near the normal region of the bow shock. This intersection results in the formation of a supersonic jet bounded between two shear layers. When the jet impinges on the surface, a jet bow shock and a small stagnation region of high pressure and high heating rates are created on the surface. It has been observed in experiments^[3] and numerical simulations^[4-7] that the type IV interaction flow is inherently unstable. This instability has strong effect on the heating rates to the body surface^[7]. The unstable mechanism, however, is currently not well understood.

The second flow problem is the interaction of a bow shock wave with free stream disturbances in hypersonic flow over a cylinder. This problem originates from the studies of receptivity to free-stream disturbances of hypersonic boundary layer. The receptivity is an important aspect of the transition from laminar to turbulent state^[8]. For hypersonic flow over a blunt body, the interaction of free-stream disturbances with the bow shock and with the acoustic waves reflected from the body produces considerable increases in the disturbance magnitudes. In order to capture more realistic situation of leading-edge receptivity of hypersonic boundary layer, such interaction should be taken into account. Morkovin^[9] assessed the flow disturbances at a blunt body owing to supersonic free-stream disturbances using a simplified one-dimensional linear analytical model, but the simplified analysis can only be applied to the disturbances along the stagnation line.

To study the transient flow phenomena in the two preceding applications, linear stability analysis the flow is difficult because of the presence of shock waves in the flow fields. In this paper, the transient hypersonic flows are studied by direct numerical simulation. Simulation of transient hypersonic flows requires numerical methods not only to capture the shock waves without spurious numerical oscillation but also to maintain high-order spatial and temporal accuracy in the smooth parts of the transient flows.

The essentially non-oscillatory (ENO) schemes^[10], which are uniformly high-order accurate shock capturing schemes, are used in this paper to perform

*Graduate Student

†Assistant Professor, Member, AIAA

the direct numerical simulations of transient hypersonic flows. The ENO schemes are chosen over the TVD schemes, which are often used in hypersonic flow calculations, because their shock capturing capability and uniform high-order accuracy away from the shock waves are particularly suitable for transient hypersonic flow calculations. Though the TVD schemes work well for steady flow computations, they may not be appropriate for transient hypersonic flow calculations because they reduce to first-order accuracy at local extrema of the smooth parts of the solutions even though they are high-order accurate elsewhere. On the other hand, the ENO schemes, in principle, can resolve discontinuity well and can achieve uniformly high-order accuracy when the flow is smooth. These properties of ENO schemes seem to be ideal for the direct simulation of transient hypersonic flow. The ENO schemes have been applied to many fluid flow problems. Examples of these applications can be found in Refs. [11–16] and [7].

There is still an uncertainty concerning the ENO schemes. The ENO schemes use a polynomial reconstruction procedure based on an adaptive stencil to avoid interpolating flow variables across discontinuities. As a result, the ENO schemes are nonlinear even when they are solving linear equations. Rogerson and Meiburg^[17] showed that the ENO schemes lose their accuracy when calculating linear wave equation with certain initial conditions. Shu^[18] consequently showed that this unnecessary loss of accuracy can be avoided by modifying the selection algorithm for interpolation stencil. However, the previous studies on validating the numerical accuracy of the ENO schemes have been mainly conducted to convective wave equations. The effect of accumulation of numerical errors of the nonlinear ENO schemes for viscous flow calculation needs to be further tested.

Therefore, the objectives of the studies in this paper are:

1. We will test the numerical accuracy of the ENO schemes for solving a model convection-diffusion equation and for solving the Navier-Stokes equations by grid refinement studies. The ENO schemes are based on the finite volume method for solving the Navier-Stokes equations, and are high-order accurate both in inviscid and in viscous terms.
2. We will continue the work of Ref. [7] to study the unsteady mechanism of the type IV shock-shock interference heating problem. The ENO schemes of third-order accuracy in space and in time are used. The unsteady mechanism of the type IV interference heating problem will be investigated by numerical simulation of unsteady flow at different Reynolds numbers. The distributions of surface

pressure and heating rates on the body surface will be compared with available experimental results in Ref. [3].

3. We will study transient hypersonic flows with free-stream acoustic disturbances over a circular cylinder at various Mach numbers and frequencies. Numerical solutions along the stagnation line will be compared with analytical results in Refs. [9, 19]. The effect of the bow shock on the disturbance field will be studied.

Governing Equations and Numerical Formulation

Details of the finite volume high-order accurate ENO schemes for the two-dimensional Euler and Navier-Stokes equations can be found in Refs. [13] and [7]. High-order approximation of both inviscid and viscous terms of Navier-Stokes equations is used in the present study.

Governing Equations

The two-dimensional Navier-Stokes equations written in the conservation-law form in Cartesian coordinates are

$$\frac{\partial U}{\partial t} + \frac{\partial F_e}{\partial x} + \frac{\partial F_v}{\partial x} + \frac{\partial G_e}{\partial y} + \frac{\partial G_v}{\partial y} = 0, \quad (1)$$

where $U = [\rho, \rho u, \rho v, e]^T$, and

$$F_e = \begin{bmatrix} \rho u \\ \rho u^2 + p \\ \rho uv \\ (e + p)u \end{bmatrix}, \quad F_v = \begin{bmatrix} 0 \\ \sigma_{11} \\ \sigma_{12} \\ \sigma_{11}u + \sigma_{12}v + q_1 \end{bmatrix},$$

$$G_e = \begin{bmatrix} \rho v \\ \rho uv \\ \rho v^2 + p \\ (e + p)v \end{bmatrix}, \quad G_v = \begin{bmatrix} 0 \\ \sigma_{21} \\ \sigma_{22} \\ \sigma_{21}u + \sigma_{22}v + q_2 \end{bmatrix}, \quad (2)$$

$$e = \frac{p}{\gamma - 1} + \frac{\rho}{2}(u^2 + v^2). \quad (3)$$

The viscous stress and heat flux terms are given by

$$\sigma_{ij} = -\mu \left(\frac{\partial u_i}{\partial x_j} + \frac{\partial u_j}{\partial x_i} - \frac{2}{3} \delta_{ij} \frac{\partial u_k}{\partial x_k} \right), \quad q_i = -\kappa \frac{\partial T}{\partial x_i}, \quad (4)$$

where μ is determined by the Sutherland's law, and κ is determined by assuming a constant Prandtl number.

Finite Volume Formulations

In the finite volume method, the integral form of conservation laws can be written as

$$\frac{\partial}{\partial t} \int_V U dV + \int_S \vec{F} \cdot d\vec{S} = 0. \quad (5)$$

Applying the above formula to a cell (i, j) located in the domain of $[x_{i-1/2}, x_{i+1/2}] \times [y_{j-1/2}, y_{j+1/2}]$, we will obtain

$$\frac{\partial \bar{U}_{ij}}{\partial t} + \frac{1}{A_{ij}} (\tilde{F}_{i+\frac{1}{2},j} - \tilde{F}_{i-\frac{1}{2},j} + \tilde{G}_{i,j+\frac{1}{2}} - \tilde{G}_{i,j-\frac{1}{2}}) = 0, \quad (6)$$

where \bar{U}_{ij} is the cell average value of U over the cell (i, j) , and $\tilde{F}_{i\pm\frac{1}{2},j}$ and $\tilde{G}_{i,j\pm\frac{1}{2}}$ are flux integrals at interfaces $S_{i\pm\frac{1}{2},j}$ and $S_{i,j\pm\frac{1}{2}}$ respectively.

The spatial accuracy of the finite-volume discretized equation depends on the numerical approximation of flux integrals. Let \tilde{F} and \tilde{G} denote the numerical fluxes which approximate \bar{F} and \bar{G} to $(r+1)$ -th order of accuracy. We can approximate the integrations by Gaussian quadrature,

$$\hat{F}_{i\pm\frac{1}{2},j} = \Delta y_j \sum_{k=1}^N \omega_k F(x_{i\pm\frac{1}{2}}, y_k, t), \quad (7)$$

where $(x_{i\pm\frac{1}{2}}, y_k)$ are locations of the Gaussian-quadrature points at interface $S_{i\pm\frac{1}{2},j}$ and ω_k are weights of Gaussian quadrature. For r -th order finite-volume scheme, we use N -point Gaussian quadrature if $2N - 1 \leq r \leq 2N$.

To evaluate the numerical fluxes at Gaussian quadrature points that are at the interface between two different cells, we apply different methods for inviscid and viscous flux terms. For inviscid flux vectors, we need to deal with the discontinuities of conservative variables at the interface by solving a Riemann problem. Since to solve a complete set of non-linear equations for the Riemann problem is very time-consuming, Roe's approximate Riemann solver^[20] is used in this paper. It has been shown that the Roe's approximate Riemann solver may not satisfy entropy condition in calculating flows with sonic transition. To avoid nonphysical solutions, we use the entropy correction of Harten and Hyman^[21] in the Roe schemes. For viscous flux vectors, we apply central difference formulas using the pointwise values of flow variables at adjacent cells to approximate the first-order derivatives of velocity and temperature.

ENO Reconstruction

In order to implement Roe's approximate Riemann solver, we need to evaluate the conservative variables, which are U_L and U_R , at the left and right sides of a cell interface. The ENO reconstruction achieves uniformly high-order accuracy by adaptively interpolating through the "smoothest" stencils to reconstruct pointwise values from cell average values. This adaptive interpolation avoids undesired oscillation near discontinuities. Details of the finite-volume ENO reconstruction can be found in Refs. [10] and [13].

Rogerson and Meiburg^[17] showed that the ENO schemes may lose high-order accuracy even though the

solution is smooth. The loss of accuracy is due to the selection of the linear unstable stencils by the original adaptive stencil-choosing algorithm of the ENO schemes. Shu^[18] proposed a modification of ENO schemes to maintain the order of accuracy of the schemes. The basic idea of this modification is to bias the adaptive stencils toward the linear stable central ones wherever the solution is smooth. The Shu's modification is used in this paper.

Evaluation of Viscous Flux Terms

We use central difference formulas to evaluate the viscous terms at the cell interfaces. The recent work of Zhong^[7] adopted central difference formulas using cell-average values of flow variables at centroids to approximate the viscous terms. This will lead to a second-order accurate scheme for the viscous terms even if the approximation of inviscid fluxes is high-order accurate. Thus, we improve the accuracy of the work in Ref. [7] by applying high-order finite difference formulas to approximate the viscous terms. For instance, we can use the following fourth-order difference formula to approximate the viscous terms as following

$$\frac{\partial u}{\partial x} \Big|_{i+\frac{1}{2}} = \frac{1}{24\Delta x} (u_{i-1} - 27u_i + 27u_{i+1} - u_{i+2}) + O(\Delta x)^4, \quad (8)$$

where u_{i-1} , u_i , u_{i+1} and u_{i+2} are the point values at cell centroids obtained by high-order ENO reconstruction from cell-average values. While approximating viscous terms near the boundaries of a computational domain, one-sided difference formulas are used to maintain the same order of accuracy.

Time Discretization

For unsteady flow computations, the accuracy in time is as crucial to the resolution of flows as the accuracy in space. For transient hypersonic flows, explicit TVD Runge-Kutta time-stepping schemes^[11] are used to achieve high-order accuracy in time.

Curvilinear Coordinates

In order to simulate realistic fluid problems with arbitrary geometry, we need to extend the study of ENO schemes to arbitrary geometry by a coordinate transformation.

Boundary Conditions

Non-slip boundary conditions with an isothermal wall are used. For inviscid fluxes at wall, we only need the wall pressure that are determined by the ENO reconstruction from the interior of flow field. At supersonic upstream of the flow boundary, we set the flow variables to the known free-stream values. At supersonic outflows, all the values of conservative variables are extrapolated from the interior of the computational domain.

Accuracy of ENO Schemes

Linear Convection-Diffusion Equation

In order to test the numerical accuracy of the ENO schemes for solving the Navier-Stokes equations, we consider the following linear convection-diffusion equation

$$\frac{\partial u}{\partial t} + c \frac{\partial u}{\partial x} = \mu \frac{\partial^2 u}{\partial x^2} \quad (9)$$

with initial condition

$$u(x, 0) = \sin^4 \pi x . \quad (10)$$

The exact solution of the initial value problem can be obtained easily for comparison. The is the test case that the numerical results of the linear wave equation by using the original ENO schemes were shown to lose order of accuracy^[17, 18]. We set $c = 1$ and $\mu = 5 \times 10^{-3}$ in the computational domain $-1 \leq x \leq 1$. The Reynolds number of this convective-dissipative problem is

$$Re = \frac{cL}{\mu} = 400. \quad (11)$$

In the case of a very large Reynolds number, the linear model equation is reduced to the linear wave equation. Therefore, the results of numerical accuracy study will be similar to those in Refs. [17, 18] if Re is very large, i.e., the ENO schemes need modification for accuracy considerations.

We computed the solutions of the present moderate Re case using the ENO code for one period in time, i.e., at $t = 2$, with CFL = 0.1 (based on CFL = $c\Delta t/\Delta x$). We performed the numerical accuracy studies on six consecutively refined grids for ENO schemes from first to sixth order accurate. For the ENO schemes with spatial accuracies less or equal to four, the computations were advanced in time by the TVD Runge-Kutta schemes of the same order in time as in space. For fifth and sixth-order ENO schemes, the computations were advanced in time by the same fourth-order TVD Runge-Kutta schemes. The number of iterations was large enough to achieve a significant accumulation of error both in time and in space. The errors are computed at the cell center in L_1 norm,

$$L_1 = \frac{1}{N} \sum_{i=1}^N |u(x_i) - u_{\text{exact}}(x_i)|. \quad (12)$$

Results of both the ENO and modified ENO schemes are shown in Tables 1 and 2, where r_c denotes the computational order of accuracy as

$$r_c = \log_2 \frac{(L_1)^{2N}}{(L_1)^N}. \quad (13)$$

Figure 1 shows the L_1 norm as a function of the numbers of grid points. The results show that the ENO schemes without modification do not lose accuracy as described in Ref. [17]. This may be due to the fact that

when the ENO schemes are applied to the model equation above, the existence of viscous term damps out the propagating wave. Figure 2 shows the results of first to sixth-order ENO schemes using 40 grid points compared with the exact solution. We can see the benefits of high-order ENO schemes for this transient problem because of low dissipative effect for ENO schemes.

Relevant to hypersonic wall-bounded flows, we next tested the accuracy of the ENO schemes in an initial-boundary value problem of the same equation with the following boundary conditions:

$$u(0, t) = 0, \quad u(l, t) = 0. \quad (14)$$

The solution of Eq. (9) with the boundary conditions above is composed of a set of eigenfunctions $\phi_n(x)$ as follows:

$$u(x, t) = \sum_{n=1}^{\infty} A_n e^{k_n t} \phi_n(x) \quad (15)$$

where

$$k_n = -\frac{1}{4\mu} \left[\left(\frac{n\pi\mu}{l} \right)^2 + c^2 \right], \quad \phi_n = e^{\frac{c}{2\mu}x} \sin \frac{n\pi}{l}x,$$

$$A_n = \frac{2}{l} \int_0^l f(x) e^{-\frac{c}{2\mu}x} \sin \frac{n\pi}{l}x dx, \quad (16)$$

and $f(x)$ is the initial condition, i.e., $u(x, 0) = f(x)$.

In the computations, we chose initial condition $f(x)$ to be eigenfunctions ϕ_m . The exact solution is

$$u(x, t) = e^{k_m t} \phi_m. \quad (17)$$

The modified fourth-order ENO scheme was used to solved the initial-boundary value problem. We set $c = 1$, $\mu = 1$ and $l = 2$. Solutions were obtained at $t = 0.05$ with CFL number based on inviscid variables to be 0.001. Table 3 shows the results of modes $m = 2$ and $m = 6$. Figures 3 and 4 show the comparison between numerical and exact solutions. The modified ENO schemes perform well for this initial-boundary value problem.

Stokes Oscillating Plate

We next computed unsteady flow over an oscillating flat plate using the third-order ENO scheme. This problem can test the ability of our numerical schemes to accurately simulate an unsteady fluid motion subject to both initial and boundary conditions. The semi-infinite fluid is at rest initially, and is set into motion when the solid plate at $y = 0$ begins to oscillate with velocity given by

$$u_{\text{plate}} = u_0 \sin \omega t. \quad (18)$$

The exact solution of this problem can be found in Ref. [22].

Although this is a one-dimensional problem, we implemented fully two-dimensional Navier-Stokes calculation so that we could compare our numerical results

with exact solution. Flow parameters were chosen to match the test condition in Rogers and Kwak^[23]. The dimensionless frequency was set to unity. The velocity u_0 was set to 40 m/s. Periodic boundary condition was used in x direction. The density, pressure, and temperature were assumed to be constant at both the wall and far field.

Figure 5 shows numerical results at the end of the computations of nine periods using twenty grid points spacing from $Y = 0$ to $Y = 6$. The CFL number was 0.5. The figure shows that the numerical solutions agree well with the exact solution. The results indicate that high-order accurate ENO schemes have good potential in simulating transient viscous flow involving an unsteady solid wall. Figure 6 shows the results at $t = 0.5$ in which the initial transient solution can not be neglected. We performed the grid refinement study through 10, 20, 40 and 80 grids in y direction. Table 4 shows the absolute error computed for each case and indicates a discrepancy in asymptotic order of accuracy. By carefully examining our numerical solutions, we found that there are some small disturbances in density, temperature and pressure, which should be constant from theoretical study. These disturbances may result from the non-linear calculations of fluxes because we computed the full Navier-Stokes equations by the non-linear ENO schemes. The source of these disturbances is not fully resolved by the current work and needs further investigation in the future.

Type IV Shock Interference Heating Problem

Figure 7 shows a schematic of type IV interference heating flow field, which was found to be inherently unstable due to the interaction among supersonic jet, shear layer, bow shock and impinging shock^[3, 4, 5, 6, 7]. In this paper, the instability mechanism of the type IV shock interference problem was investigated by numerical simulation of laminar hypersonic flow using the explicit ENO schemes with third-order accuracy in time and space. The effect of Reynolds number was studied numerically. Three test cases with different Reynolds numbers were studied using both coarse grids (96×61) and fine grids (192×122) to examine numerical accuracy of solutions. Flow conditions of the three test cases are given in Table 5. The first test case was chosen to be the same as case S0 in Thareja et al.^[5] and the experimental results^[3] are available for comparison. Meanwhile, the accuracy of the numerical results was also examined by grid-refinement studies.

High Reynolds Number Flow

Reynolds number of the first test case was 2.57×10^5 . The CFL number of 0.95 was used in the explicit calculations. The computational grids shown in Fig. 8 are the same as those used in Ref. [7].

Figure 9 shows the time histories of maximum surface pressure and its location measured by the angle from the horizontal position. The results shown in this paper are those obtained using the fine 192×122 grids. Figure 10 shows the comparison of instantaneous surface pressure and heating rates with experimental results. The surface pressure and heating rates were normalized by p_0 and q_0 ($p_0/p_\infty = 83.5$ and $q_0 = 41.43 \text{ Btu/ft}^2\text{s}$). The inherent unsteadiness can be observed from the figures by examining the location and magnitude of maximum surface pressure. Compared with experimental results, the present numerical solutions overpredict the peak pressure and underpredict the peak heating rates. This discrepancy between experimental and numerical results could result from the real gas effects at high temperature and the possible free-stream disturbances in the experiment.

Figure 11 shows the instantaneous temperature contours of the flow field. We can observe that our numerical schemes have well resolved the transmitted shock, supersonic jet, shear layers and boundary layer. The separation of boundary layer on the upper cylinder is due to viscous interaction of a reflected shock with the boundary layer. The separation on the lower cylinder may result from the significantly spatial oscillation of surface pressure shown in Fig. 10.

Various studies on different free-stream Mach numbers have been done experimentally and numerically. The basic unsteady flow pattern is similar. The Reynolds number for those tests is high enough to result in possible transition from laminar to turbulent states in the boundary layer. This might have a feedback to the unsteadiness of flow pattern and enhance the instability of the interference flow which has also been observed in Ref. [7]. In order to study the effect of Reynolds numbers on the unsteadiness the the present flow, the numerical simulations were conducted at the same free-stream Mach number with lower Reynolds numbers. The results are presented in the next two test cases.

Medium Reynolds Number Flow

Reynolds number of the second test case was 2.57×10^3 . The free-stream Mach number and temperature were the same as those of the previous test case. The impinging shock was generated at the same location with the same strength and angle. A set of different grids was used with fewer points clustered near the boundary than the previous case because the boundary layer was thicker. The numerical accuracy of the results were tested by grid refinement study using both coarse (96×61) grids and fine (192×122) grids.

Figure 12 shows the time histories of maximum surface pressure and its location on the cylinder surface based on the results using the fine grid. Figure 13 shows the distribution of surface pressure and heating rates. Since no experimental data were available for

comparison, we normalized the surface pressure and heating rates by the same factors as previous test case. In the present test case of lower Reynolds number, the oscillation of peak pressure was restrained within a rather small range, and the location of peak pressure did not slide along the cylinder surface as it did in the previous case. The interference flow is more stable than the one with higher Reynolds number. This can be seen in Fig. 14, which shows the temperature contours. The contours are smoother than the previous ones shown in Fig. 11. This may indicate that there are fewer disturbances in the flow field at lower Reynolds number. The reflected shock pattern is significantly smeared, and no separation of boundary layer occurs on either sides of cylinder. Figure 13 indicates no spatial oscillation of pressure along the lower surface of cylinder. The peak heating rates are an order of magnitude lower than those of the previous case at a higher Reynolds number. The lower heating rates at a low Reynolds number are the results of a thicker boundary layer results in smaller gradient in temperature across the boundary layer, thus, a small heating rates on the cylinder surface.

Low Reynolds Number Flow

The Reynolds number of the third test case was 2.57×10^2 . Figures 15, 16 and 17 show the numerical results using the 192×122 fine grids. We can observe that the interference flow in this case is the most stable one among the three test cases. In Fig. 16, the supersonic jet, shear layer as well as the jet bow shock are significantly smeared to a further extent than those in the second test case. The bow shock is much thicker than those of the previous two test cases because the Knudson number for the present case is about 10^{-2} , which is much higher than those of previous cases. The distribution of surface pressure and heating rates are quite smooth, and peak values are much lower than those of the previous test cases. This may be due to the fact that the reduction in the strength of the jet bow shock results in a less compression on the cylinder surface and smaller peak values of surface pressure and heating rates. Moreover, a larger boundary layer thickness should also contribute to the reduction of the peak surface heating rates for the present case.

Based on the observation of our numerical simulations, the unsteadiness of high and low Reynolds numbers for type IV interference heating depends strongly on the Reynolds numbers of the flow. In order to gain more insight into the unsteady mechanism of the type IV interference flow, studies in the real gas effects and the effect of free-stream disturbances to the onset of instability of the flow are needed in the future.

Shock-Disturbance Interaction for Hypersonic Flow over a Cylinder

In order to study the detailed structure of flow disturbances outside the hypersonic boundary layer, we conduct direct numerical simulation of free-stream planar acoustic waves interacting with the bow shock in front of a cylinder moving at hypersonic speeds. Fig. 18 shows a schematic of the flow field. In the numerical simulation, the Euler equations were solved by the high-order ENO schemes. The numerical solutions were compared with results of the one-dimensional analysis by Morkovin^[9] for the flow field downstream of the bow shock. The time history of the pressure fluctuations behind the bow shock was also compared with linear analytical prediction by McKenzie and Westphal^[19]. Meanwhile, grid refinement studies were carried out to ensure the numerical accuracy of the numerical solutions.

Linear Analysis

The case for a single upstream entropy wave has been analyzed by Morkovin^[9]. In this paper, we consider the case of acoustic wave/shock interaction. We use the same notations those of Ref. [9] in the linear analysis. Following the analysis by Morkovin, the analytical solutions for acoustic wave/shock interaction along the stagnation line can be formulated approximately as a one-dimensional problem shown in Fig. 19. In order to simplify the analysis, the bow shock is assumed to be a normal one. The mean flow properties between the shock and the body are assumed to be uniform. The disturbance pressure, density, and entropy are nondimensionalized by the local steady-state properties as follows:

$$p(\pm) = \frac{\delta p}{\gamma p} \quad u(\pm) = \frac{\delta u}{c} \quad s(\pm) = \frac{\delta S}{C_p}, \quad (19)$$

where c is speed of sound, and C_p is the specific heat at constant pressure. Disturbances from the mean flow of flow variables upstream and downstream of the bow shock are denoted by subscripts of minus and plus signs respectively. Upstream mean flow properties are distinguished from the downstream ones by subscript 1. The upstream disturbances are assumed to be a planar acoustic wave with a single frequency, i.e.,

$$\begin{aligned} p_- &= A_{p_-} e^{i\omega[t - \frac{x}{c_1(1+M_1)}]} , \\ u_- &= A_{u_-} e^{i\omega[t - \frac{x}{c_1(1+M_1)}]} , \\ s_- &= A_{s_-} e^{i\omega[t - \frac{x}{c_1 M_1}]} , \end{aligned} \quad (20)$$

then the disturbances behind the shock are the combination of down-stream propagating waves and up-stream propagating acoustic waves reflected from the solid surface:

$$\begin{aligned} p_+ &= A_{p_+} e^{i\omega[t - \frac{x}{c(1+M)}]} + A_{p'_+} e^{i\omega[t + \frac{x}{c(1-M)}]} \\ u_+ &= A_{u_+} e^{i\omega[t - \frac{x}{c(1+M)}]} + A_{u'_+} e^{i\omega[t + \frac{x}{c(1-M)}]} \\ s_+ &= A_{s_+} e^{i\omega[t - \frac{x}{cM}]} , \end{aligned} \quad (21)$$

where the second parts in p_+ and u_+ account for the up-stream moving acoustic wave which is reflected from the body. The shape of the bow shock is perturbed from its mean position as follows:

$$\psi = -iA_\psi e^{ijz+i\omega t}. \quad (22)$$

The unknown parameters j , l , m and n account for the phases of downstream disturbances and shock displacement. If disturbances are small, the downstream disturbances and the displacement of unsteady shock can be solved in terms of the given upstream disturbances using linearized Rankine-Huginiot's equations^[9]:

$$\begin{bmatrix} s_+ \\ p_+ \\ u_+ \end{bmatrix} - \begin{bmatrix} \Pi_{11} \\ \Pi_{21} \\ \Pi_{31} \end{bmatrix} \frac{1}{c} \frac{\partial \psi}{\partial t} = \begin{bmatrix} \Lambda_{11} & \Lambda_{12} & \Lambda_{13} \\ \Lambda_{21} & \Lambda_{22} & \Lambda_{23} \\ \Lambda_{31} & \Lambda_{32} & \Lambda_{33} \end{bmatrix} \begin{bmatrix} s_- \\ p_- \\ u_- \end{bmatrix} \quad (23)$$

where the coefficients in the matrices are the functions of upstream Mach number only and their detailed formulations can be found in Ref. [9]. From acoustic theory, the amplitudes of down-stream and up-stream moving acoustic waves satisfy

$$A_{p_+} = A_{u_+}, \quad A_{p'_+} = -A_{u'_+}. \quad (24)$$

The boundary condition on the body requires that the disturbance velocity u_+ vanishes on the body leads to

$$A'_{u_+} = -A_{u_+}, \quad l = n + \frac{2\omega d}{c(1-M^2)} + 2N\pi. \quad (25)$$

where N is an arbitrary integer. The unknowns s_+ , p_+ and u_+ can be solved from the system of three complex equations (23).

For the present case of an acoustic wave in the free stream, s_- is zero. Solving Eq. (23) gives us the pressure perturbation

$$\frac{p_+}{A_{u_-}} e^{-i\omega[t + \frac{x}{c(1-M)}]} = \frac{\Omega_{23}}{P_{23} e^{\frac{2i\omega d}{c(1-M^2)}} - P_{23}^+} [1 + e^{\frac{2i\omega(d-x)}{c(1-M^2)}}], \quad (26)$$

where

$$\begin{aligned} P_{23}^+ &= \Pi_{21} + \Pi_{31}, & P_{23} &= \Pi_{21} - \Pi_{31}, \\ \Omega_{23} &= \Pi_{21}(\Lambda_{32} + \Lambda_{33}) - \Pi_{31}(\Lambda_{22} + \Lambda_{23}). \end{aligned} \quad (27)$$

From above relations, we can obtain the amplitudes of pressure and velocity perturbations downstream of the shock along the stagnation line. It can be shown that the pressure perturbation on the body surface is

$$\left| \frac{p_+(d)}{A_{u_-}} \right| = \frac{|2\Omega_{23}|}{[P_{23}^2 + P_{23}^{+2} - 2P_{23}P_{23}^+ \cos \frac{2\omega d}{c(1-M^2)}]^{1/2}}, \quad (28)$$

which always greater than those away from the body.

On the other hand, the initial moment after imposing the disturbances in the free stream, the disturbance

field behind the bow shock consists of downstream moving waves only until the acoustic waves reflected from the body reach the bow shock. Under such condition, the analytical solution of pressure perturbation right behind the shock can be found in Ref. [19] as

$$\left| \frac{p_+}{p_-} \right| = \frac{p}{p_1} \frac{2M_1^4 + 2(\gamma+1)M_1^3 + (3\gamma-1)M_1^2 - \gamma + 1}{(\gamma+1)(1+M_1^2 + 2MM_1^2)} \quad (29)$$

Numerical Simulation

Supersonic ideal-gas flow with free-stream acoustic disturbances over a circular cylinder was studied for test cases of several frequencies. Free-stream Mach number was set to 8.03. Radius of cylinder was 0.0381. Two sets of computational grids were used (100 × 80, 200 × 160) with uniform grid spacing in radial and tangential directions. Calculations were carried out through following procedure. First, the second-order ENO scheme was used to obtain a steady flow field. Once the steady flow was obtained, the forcing acoustic waves were superimposed on the free-stream boundary of the computational domain. For computation of unsteady flow field, the third-order ENO scheme in space with second-order explicit Runge-Kutta method in time was used.

Steady flow field

Figure 20 shows the results of mean pressure and density calculation along stagnation lines using both coarse and fine grids. Figure 21 shows the pressure contours of coarse grid computation. We can observe the shock is well captured. The third or higher-order ENO schemes are not suitable for steady flow calculation since the numerical instability becomes significant in high-order shock capturing schemes. Even though using only second-order ENO schemes, we did observe slight oscillations in the steady flow solutions. Thus, in order to understand the effect of this numerical instability on steady calculation, we calculated the mean values of numerical solutions of the steady flow field computed by the second-order ENO schemes. We then obtained the deviation of numerically solutions from their mean values by taking the root-mean-square integration. This deviation can be seen as a numerical disturbances in steady flow calculation. Figures 22 and 23 show the magnitudes of pressure and density deviations normalized by the corresponding theoretical mean stagnation properties. Figures 24 and 25 show the distributions of pressure and density deviations along the stagnation line ($\theta = 0^\circ$) and the maximum disturbance plane ($\theta = 48.6^\circ$). We can observe that maximum deviations are mainly at the shoulder of the bow shock and the magnitudes are very small. The way to control this instability is to use stronger numerical dissipation schemes (for instance, the TVD minmod limiter) to damp out the instability. However, since the levels of deviation in most part of the flow

field are small compared with the magnitude of disturbances which we introduced for unsteady calculation, the results of second-order ENO calculation for steady flow fields are acceptable for our unsteady simulation.

Acoustic wave/shock interaction

After steady flow field had been set up, we introduced acoustic disturbances at free-stream boundary. The free-stream acoustic disturbances were $\delta q = \Delta q e^{ik(x-(u+c)t)}$, where q can be u , v , p or ρ . The amplitude of acoustic wave ϵ_0 was set to be one percent of free-stream unperturbed properties as follows:

$$\begin{aligned} \Delta u &= \epsilon_0 u_\infty, & \Delta v &= 0, \\ \Delta P &= \rho_\infty c_\infty \Delta u, & \Delta \rho &= \Delta p / c_\infty^2. \end{aligned} \quad (30)$$

Three wave numbers ($k=125, 170, 250 \text{ m}^{-1}$) were chosen in such manner that the computational grids could resolve the disturbance waves downstream the shock. The CFL number was approximately 0.8. All the unsteady computations were performed for 30 disturbance periods. Calculations of root-mean-square flow quantities were carried out for the last 25 periods.

Figure 26 shows the time history of disturbance pressure at the point behind the bow shock along the stagnation line for the case of wave number $k=250$. Two discrete zones can be seen in this figure. The first zone contains a down-stream moving acoustic waves (with the speed $u+c$) only. The second one consists of both down-stream moving and up-stream moving (with the speed $u-c$) acoustic waves reflected from the wall. The straight lines in the first zone correspond to the maximum and minimum values given by Eq. (29). Since no disturbances can transmit through the shock and propagate upstream, these acoustic waves are reflected back and forth in the region between the shock and the body. Because the reflection coefficient (McKenzie et al.^[19]) of acoustic waves incident behind the normal shock can not exceed unity, the resonance of acoustic waves is not likely to build up. Nevertheless, these acoustic disturbances will reach an equilibrium state after several disturbance periods as shown in Fig. 26.

Figure 27 shows the results of root-mean-square disturbance pressure distribution along the stagnation line from both coarse and fine grid computations with wave number $k=125$. The results show that current grids are accurate enough to resolve the transient flow features. Figures 28 and 29 show the comparison of numerical solutions with analytical ones for flow at different free-stream frequencies. The solid lines correspond to the analytical values obtained from Eq. (28). The "wavelengths" from numerical calculations are slightly larger than those from analytical solutions. Amplitudes of disturbances are also greater than those predicted by analysis. This may attribute to the simplified assumption of uniform steady flow field behind the shock in the analytical analysis. In reality, the steady flow is not uniform downstream the shock. The difference in

wavelength can be easily verified as follows. If we take root-mean-square calculation with respect to time for Eq. (28), the 'wavelength' λ should satisfy

$$\frac{2\omega\lambda}{c(1-M^2)} = 2\pi. \quad (31)$$

Substitute $\omega = k(u_1 + c_1)$ for acoustic waves, we obtain

$$\lambda = \frac{\pi c(1-M^2)}{kc_1(1+M_1)}. \quad (32)$$

Since the mean flow velocity is decelerating toward the wall, the wavelength will become larger than that obtained from uniform flow assumption. This will also affect the amplitudes of disturbances, as can be verified from inspecting the one-dimensional momentum equation. The net effect is the additional amplification of disturbance properties in the numerical solutions near the wall as shown in these figures.

Figure 30 shows the contours of root-mean-square disturbance pressure, density and vorticity with $k=250$. The results show maximum disturbance pressure at the stagnation point. Amplitudes of disturbances drop an order of magnitude as these disturbances propagate away from the stagnation line. Other numerical results using different free-stream Mach number show the similar trend. Figure 30(c) shows that the maximum disturbance vorticity is generated near the shoulder of the curved bow shock. This indicates that most of the vorticity waves generated downstream of the shock due to the upstream shock/acoustic wave interaction are away from the body.

Figure 31 shows the contours of instantaneous disturbance pressure, density and vorticity. The amplified acoustic wave pattern can be observed in Fig. 31(a). Since the disturbance density field is composed of both acoustic and entropy waves, the flow pattern is not so clear as that shown in Fig. 31(a). However, two zones downstream of the shock can be roughly seen. The first zone, which is near the shock, is composed of both acoustic and entropy waves. The second one, which is near the body, is mainly composed of acoustic waves. The entropy waves seem to be smeared near the body. The unsteady flow pattern and enlarged flow disturbances near the stagnation region might have substantial influence on boundary layer transition. Therefore, the numerical results of present work will be valuable in the understanding the effect of shock/disturbances interaction on hypersonic boundary layer transition. The results of the present test case also show that the uniform acoustic waves become very nonuniform in magnitude after the interaction with the bow shock and with the reflected waves from the cylinder. This demonstrates importance of including the bow shock wave as part the flow field in the direct numerical simulation of receptivity of hypersonic boundary layer.

Conclusions

The high-order accurate ENO schemes have been applied to two-dimensional compressible Euler and Navier-Stokes equations for studying transient hypersonic viscous flows. The accuracy of the ENO schemes has been tested by the grid refinement studies on the linear convection-diffusion equation. Numerical results of Stokes oscillating plate indicate that the high-order ENO schemes have good ability to calculate the unsteady fluid flows with solid boundaries.

The type IV shock interference heating problem has been studied by applying high-order ENO schemes to hypersonic viscous flows at different Reynolds numbers. The inherent unsteadiness of the flow has been captured by third-order accurate ENO schemes for the Navier-Stokes equations. Numerical results show that the Reynolds number has a strong effect on the instability of the interference flow. The flow becomes more and more stable when the Reynolds numbers decrease.

The interaction of small free-stream disturbances with bow shock wave in front of a cylinder has been studied through different disturbance frequencies. Intense amplification of disturbances downstream of the shock was found in both analytical and numerical studies. Numerical results show reasonable agreement with a simplified analytical solution. The acoustic waves become very nonuniform in magnitude near the cylinder, which shows the importance of including the bow shock wave as part the flow field in the direct numerical simulation of receptivity of hypersonic boundary layer.

Acknowledgement

This research was supported by the Air Force Office of Scientific Research Grant F49620-92-J-0090 and F49620-94-1-0019 monitored by Dr. Leonidas Sakell.

Reference

- [1] National Research Council (U.S.). Committee on Hypersonic Technology for Military Application, *Hypersonic technology for military application*, Technical report, 1989.
- [2] Edney, B., Anomalous heat transfer and pressure distributions on blunt bodies at hypersonic speeds in the presence of an impinging shock, FFA Report 115, Aeronautical Research Institute of Sweden, 1968.
- [3] Wieting, A. R. and Holden, M. S., Experimental shock-wave interference heating on a cylinder at Mach 6 and 8, *AIAA Journal*, Vol. 27, Nov. 1989, pp. 1557-1565.
- [4] Klopper, G. H. and Yee, H. C., Viscous hypersonic shock-on-shock interaction on blunt cowl lips, AIAA Paper 88-0233.
- [5] Thareja, R. R., Stewart, J. R., Hassan, O., Morgan, K., and Peraire, J., A point implicit unstructured grid solver for the Euler and Navier-Stokes equations, *International J. for Numerical Methods in Fluids*, Vol. 9, 1989, pp. 405-425.
- [6] Gaitonde, D. and Shang, J. S., The performance of flux-split algorithms in high-speed viscous flows, AIAA Paper 92-0186.
- [7] Zhong, X., Application of high-order ENO schemes to unsteady hypersonic shock-shock interference heating on a cylinder, *AIAA Journal*, Aug. 1994, pp. 1606-1616.
- [8] Choudhari, M. and Streett, C., Boundary Layer Receptivity Phenomena in Three-Dimensional and High-Speed Boundary Layers, AIAA Paper 90-5258.
- [9] Morkovin, M. V., Note on the Assessment of Flow Disturbances at a Blunt Body Traveling at Supersonic Speeds Owing to Flow Disturbances in Free Stream, *J. of Applied Mechanics*, Vol. 27, 1960, pp. 223-229.
- [10] Harten, A., Engquist, B., Osher, S., and Chakravarthy, S., Uniformly high order accurate essentially non-oscillatory schemes, III, *J. of Computational Physics*, Vol. 71, 1987, pp. 231-303.
- [11] Shu, C. and Osher, S., Efficient implementation of essentially non-oscillatory shock-capturing schemes, *J. of Computational Physics*, Vol. 77, 1988, pp. 439-471.
- [12] Shu, C. and Osher, S., Efficient implementation of essentially non-oscillatory shock-capturing schemes, II, *J. of Computational Physics*, Vol. 83, 1989, pp. 32-78.
- [13] Casper, J., Essentially non-oscillatory shock-capturing schemes to multi-dimensional systems of conservation laws, PhD thesis, Old Dominion University, Dec. 1990.
- [14] Shu, C., Erlebacher, G., Zhang, T. A., Whitaker, D., and Osher, S., High-order ENO schemes applied to two- and three-dimensional compressible flow, CAM Report 91-09, Department of Mathematics, University of California, Los Angeles, 1991.
- [15] Atkins, H. L., High-order ENO methods for the unsteady compressible Navier-Stokes equations, AIAA Paper 91-1557.

- [16] Casper, J. and Atkins, H. L., A finite-volume high-order ENO scheme for two-dimensional hyperbolic systems, *J. of Computational Physics*, Vol. 106, 1993, pp. 62-76.
- [17] Rogerson, A. M. and Meiburg, E., A numerical study of the convergence properties of ENO schemes, *J. of Scientific Computing*, Vol. 5, No. 2, 1990, pp. 151-167.
- [18] Shu, C., Numerical experiments on the accuracy of ENO and Modified ENO schemes, *J. of Scientific Computing*, Vol. 5, No. 2, 1990, pp. 127-149.
- [19] Mckenzie, J. F. and Westphal, K. O., Interaction of Linear Waves with Oblique Shock Waves, *Physics of Fluids*, Vol. 11, No. 11, 1968, pp 2350-2362.
- [20] Roe, P. L., Approximate Riemann solvers, parameter vectors, and difference schemes, *J. of Computational Physics*, Vol. 43, 1981, pp. 357-372.
- [21] Harten, A. and Hyman, J. M., Self adjusting grid methods for one-dimensional hyperbolic conservation laws, *J. of Computational Physics*, Vol. 50, 1983, pp. 235-269.
- [22] Panton, R. L., *Incompressible Flow*, John Wiley & Sons Inc., 1984.
- [23] Rogers, S. E. and Kwak, D., Upwind differencing scheme for the time-accurate incompressible Navier-Stokes equation, *AIAA Journal*, Vol. 28, Feb. 1990, pp. 253-262.

Table 1: Solution errors of ENO schemes applied to convection-diffusion equation

grid	L_1 Error (r_c)			
	3rd order ENO	4th order ENO	5th order ENO	6th order ENO
20	5.724×10^{-2}	3.004×10^{-2}	1.636×10^{-2}	1.061×10^{-2}
40	1.094×10^{-2} (2.39)	3.078×10^{-3} (3.29)	6.842×10^{-4} (4.58)	2.168×10^{-4} (5.61)
80	1.395×10^{-3} (2.97)	1.753×10^{-4} (4.13)	2.097×10^{-5} (5.03)	2.937×10^{-6} (6.21)
160	1.708×10^{-4} (3.03)	9.586×10^{-6} (4.19)	6.494×10^{-7} (5.01)	4.440×10^{-8} (6.05)
320	2.124×10^{-5} (3.01)	5.838×10^{-7} (4.04)	2.010×10^{-8} (5.01)	6.783×10^{-10} (6.03)
640	2.648×10^{-6} (3.00)	3.610×10^{-8} (4.02)	6.244×10^{-10} (5.01)	1.052×10^{-11} (6.01)

Table 2: Solution errors of modified ENO schemes applied to convection-diffusion equation

grid	L_1 Error (r_c)			
	3rd order ENO	4th order ENO	5th order ENO	6th order ENO
20	5.031×10^{-2}	2.590×10^{-2}	1.541×10^{-2}	1.061×10^{-2}
40	8.738×10^{-3} (2.53)	2.339×10^{-3} (3.47)	6.886×10^{-4} (4.48)	2.169×10^{-4} (5.61)
80	1.229×10^{-3} (2.83)	1.333×10^{-4} (4.13)	2.102×10^{-5} (5.03)	2.937×10^{-6} (6.21)
160	1.570×10^{-4} (2.97)	8.027×10^{-6} (4.05)	6.493×10^{-7} (5.02)	4.440×10^{-8} (6.05)
320	1.970×10^{-5} (2.99)	4.951×10^{-7} (4.02)	2.010×10^{-8} (5.01)	6.783×10^{-10} (6.03)
640	2.465×10^{-6} (3.00)	3.076×10^{-8} (4.01)	6.244×10^{-10} (5.01)	1.052×10^{-11} (6.01)

Table 3: Solution errors of modified fourth-order ENO scheme applied to the initial-boundary value problem

grid	L_1 Error (r_c)	
	mode $m = 2$	mode $m = 6$
20	5.071×10^{-5}	8.043×10^{-4}
40	3.091×10^{-6} (4.04)	2.575×10^{-5} (4.97)
80	1.833×10^{-7} (4.06)	1.740×10^{-6} (3.89)
160	1.089×10^{-8} (4.07)	8.868×10^{-8} (4.29)
320	6.596×10^{-10} (4.06)	4.821×10^{-9} (4.20)
640	4.100×10^{-11} (4.01)	2.856×10^{-10} (4.07)

Table 4: Solution errors of modified third-order ENO scheme for Stokes oscillating plate problem

grid	L_1 Error (r_c)
4×10	5.378×10^{-2}
8×20	8.738×10^{-3} (2.62)
16×40	4.377×10^{-3} (1.00)
32×80	2.463×10^{-3} (0.83)

Table 5: Flow conditions for type IV interference heating

Test case	1	2	3
Reynolds number	2.57354×10^5	2.57354×10^3	2.57354×10^2
Free-stream pressure (N/m ²)	985.015	9.85015	0.985015
Free-stream Mach number	8.03		
Prandtl number	0.72		
Specific heat ratio	1.4		
wall temperature (K)	294.44		
Free-stream temperature (K)	111.56		
Gas constant (N m/kg K)	286.92		
Cylinder radius (m)	0.0381		
Flow deflection angle (deg.)	12.5		
Impinging shock location (m)	(-0.00889, -0.013276)		

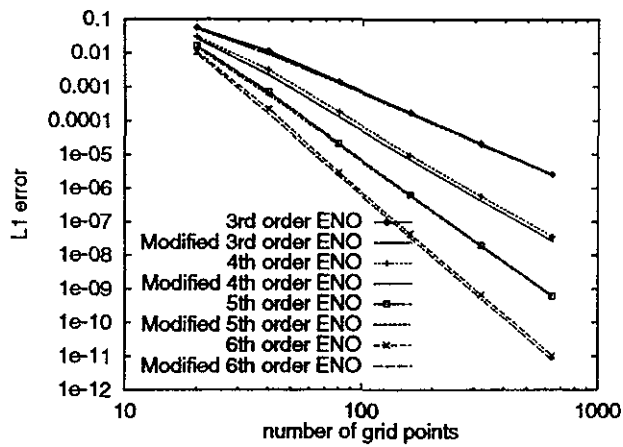


Fig. 1: Grid refinement study for convection-diffusion equation with $u(x, 0) = \sin^4 x$.

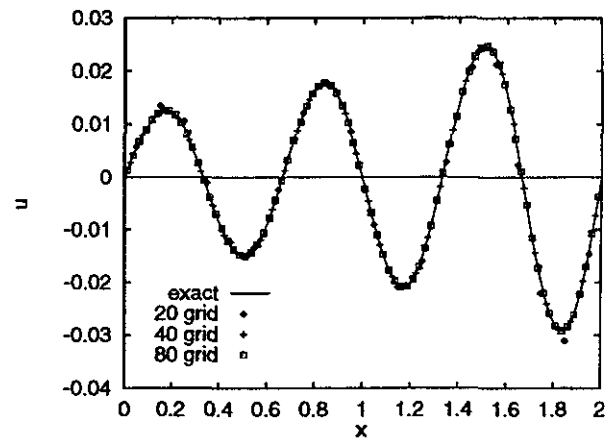


Fig. 4: Numerical solutions of convection-diffusion equation with $u(x, 0) = e^{0.5x} \sin 3\pi x$.

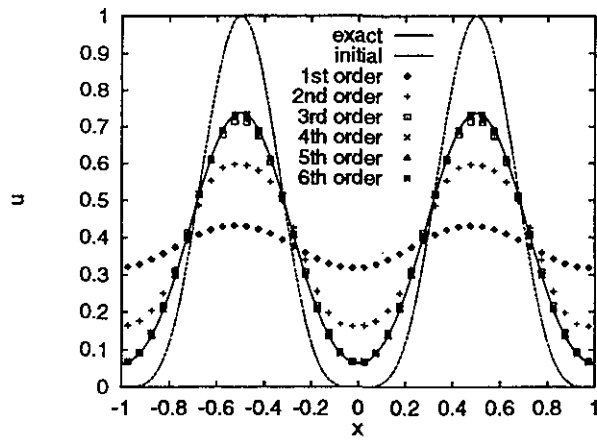


Fig. 2: Numerical solutions of convection-diffusion equation with $u(x, 0) = \sin^4 x$.

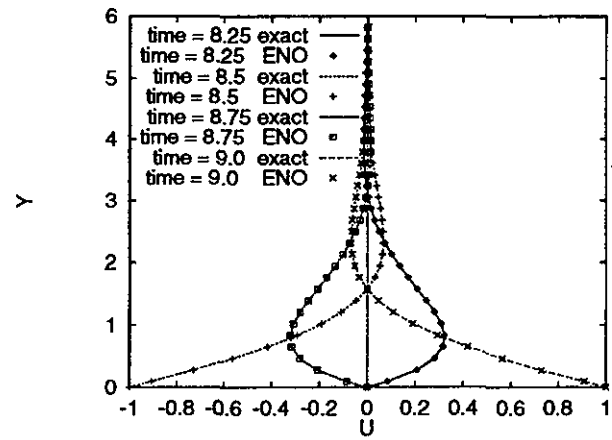


Fig. 5: Instantaneous solutions of Stokes oscillating plate at various cycles.

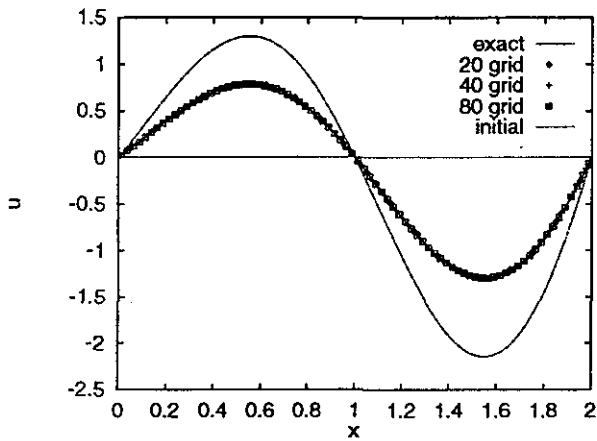


Fig. 3: Numerical solutions of convection-diffusion equation with $u(x, 0) = e^{0.5x} \sin \pi x$.

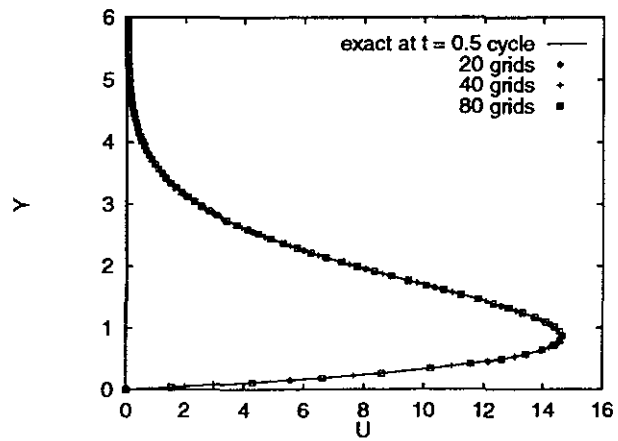


Fig. 6: Grid refinement study for Stokes oscillating plate at $t = 0.5$ cycle.

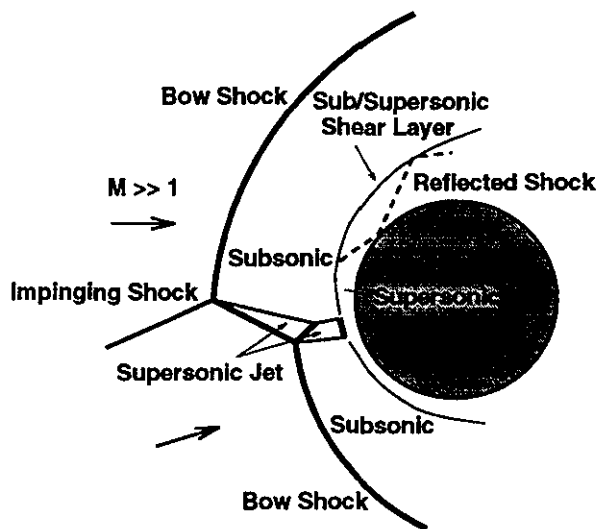


Fig. 7: Schematic of type IV shock interference flow.

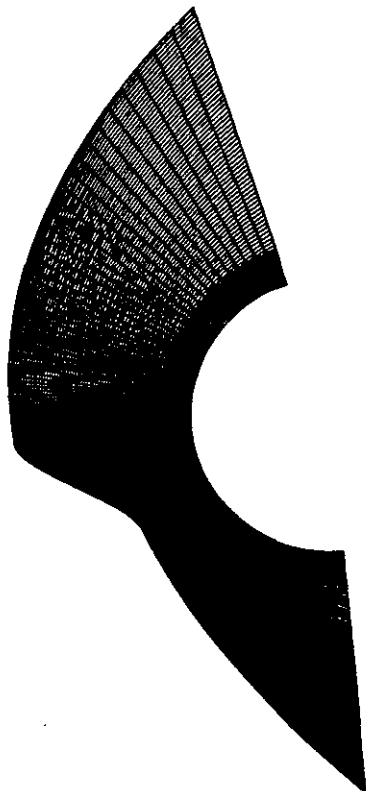


Fig. 8: Computational grids for type IV shock interference flow (192×122).

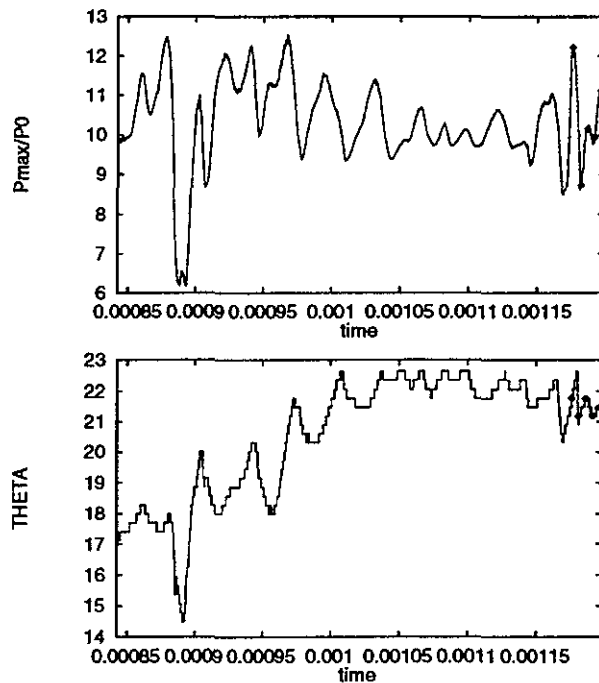


Fig. 9: Time history of magnitude and location of maximum surface pressure for type IV interference heating, $Re = 2.57 \times 10^5$.

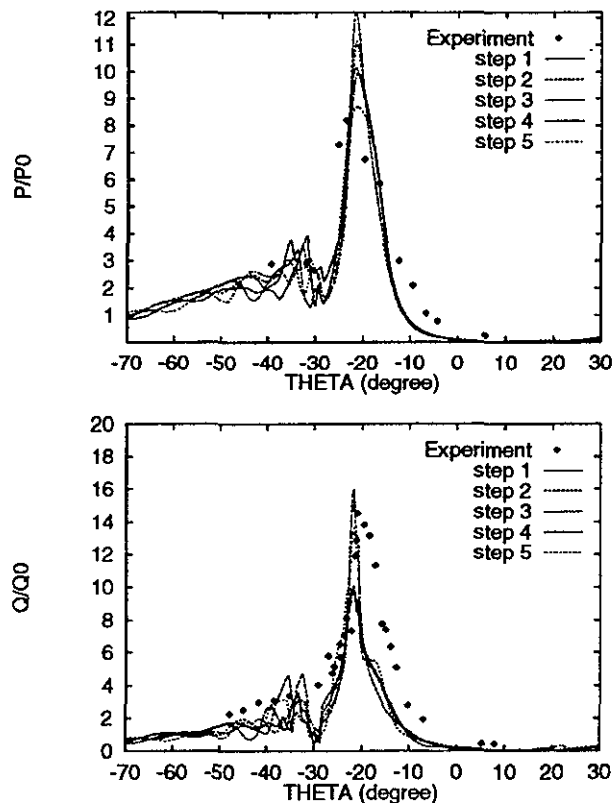


Fig. 10: Distribution of surface pressure and heating rate, $Re = 2.57 \times 10^5$.

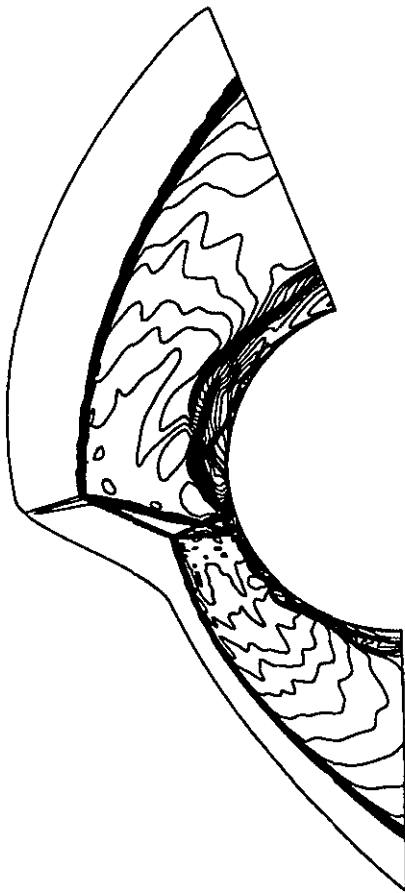


Fig. 11: Temperature contours of type IV interference heating, $Re = 2.57 \times 10^5$, fine grids (192×122).

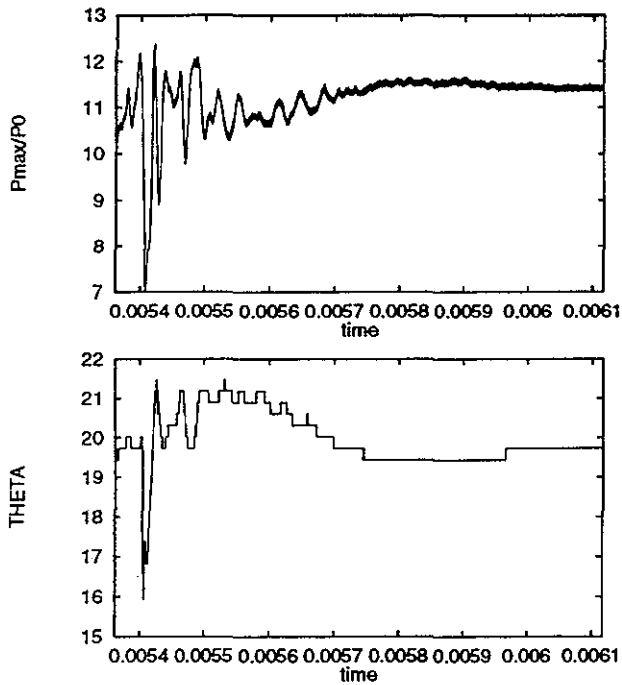


Fig. 12: Time history of magnitude and location of maximum surface pressure for type IV interference heating, $Re = 2.57 \times 10^3$.

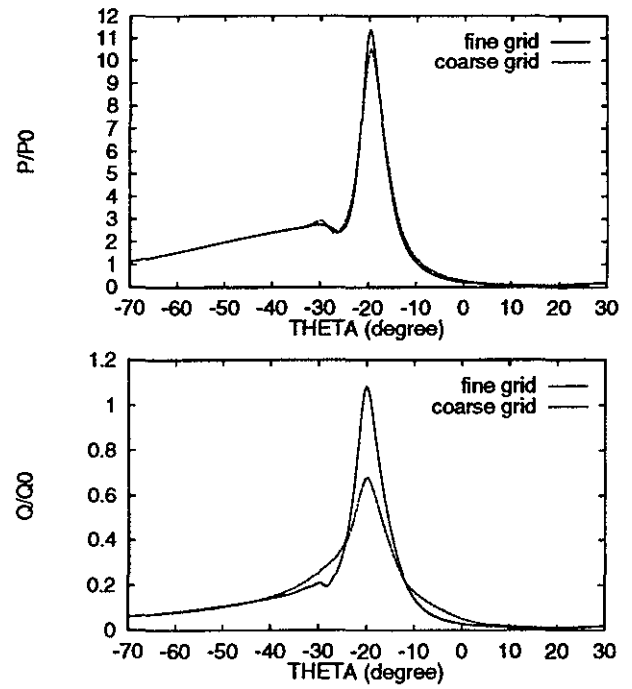


Fig. 13: Distribution of surface pressure and heating rate, $Re = 2.57 \times 10^3$.

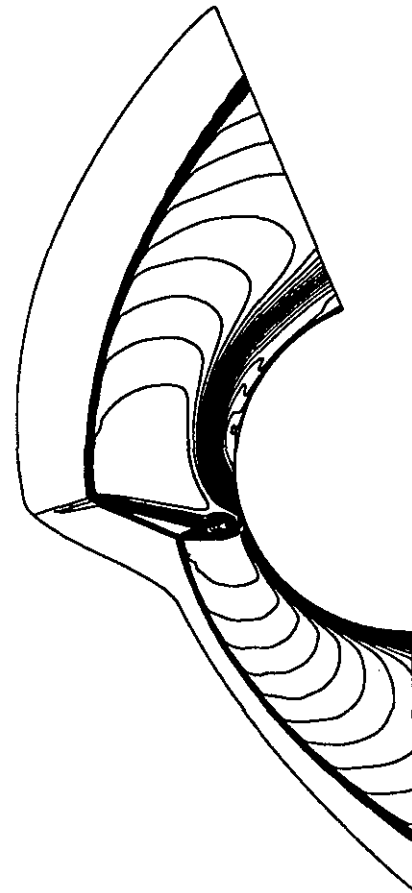


Fig. 14: Temperature contours of type IV interference heating, $Re = 2.57 \times 10^3$, fine grids (192×122).

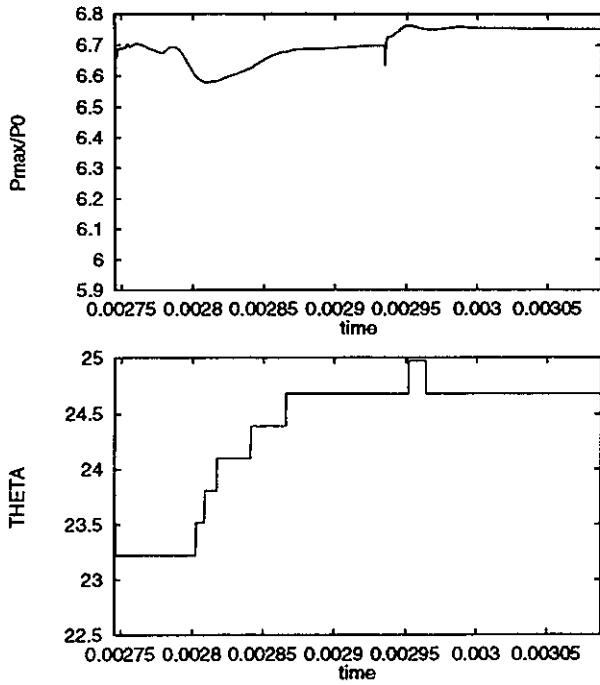


Fig. 15: Time history of magnitude and location of maximum surface pressure for type IV interference heating, $Re = 2.57 \times 10^2$.

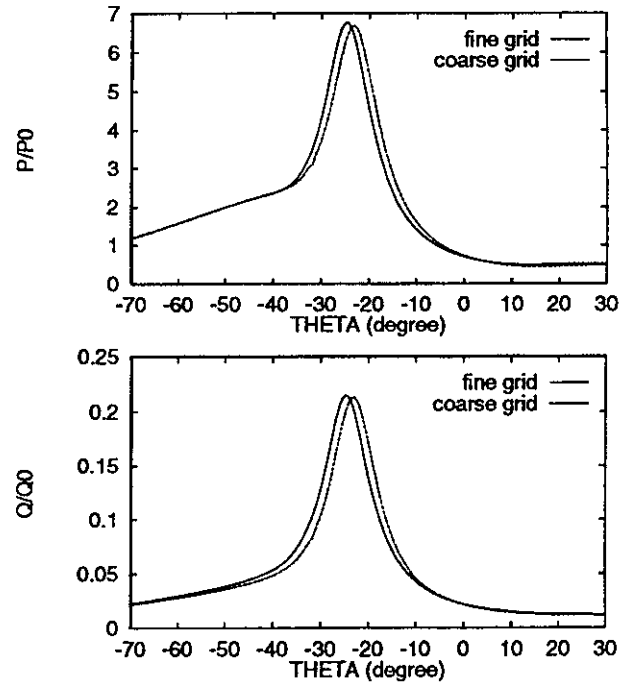


Fig. 17: Distribution of surface pressure and heating rate, $Re = 2.57 \times 10^2$.

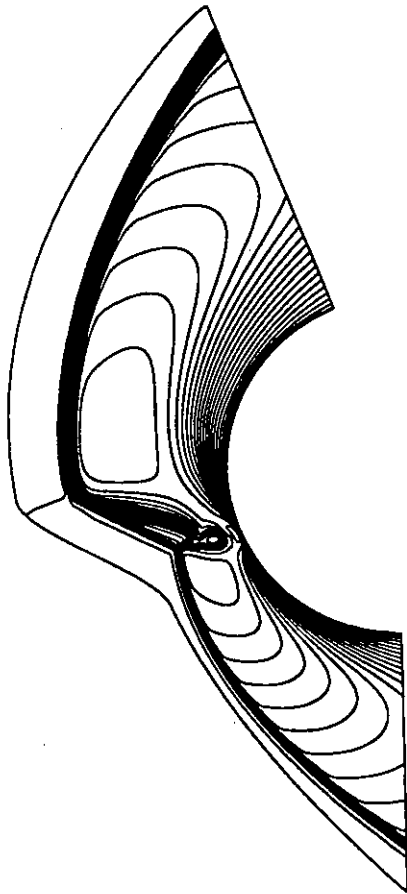


Fig. 16: Temperature contours of type IV interference heating, $Re = 2.57 \times 10^2$, fine grids (192×122).

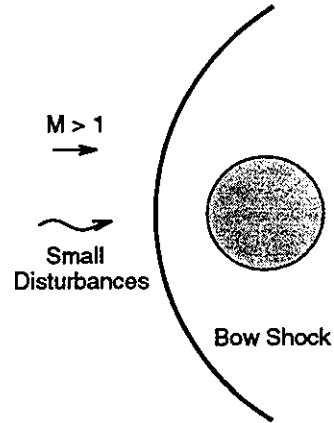


Fig. 18: Schematic of shock/disturbance interaction for hypersonic flow over a cylinder.

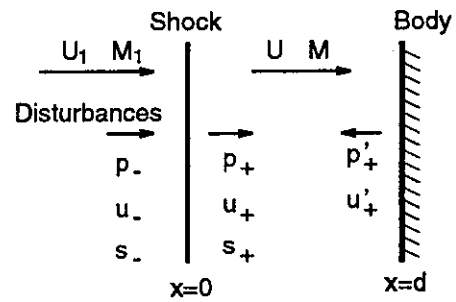


Fig. 19: One-dimensional assumption by Morkovin^[9] for shock/disturbance interaction.

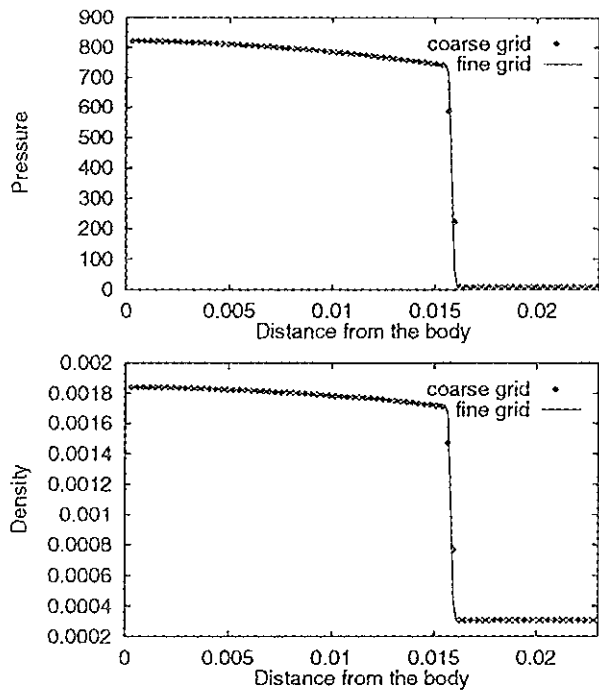


Fig. 20: Distribution of mean pressure and density along the stagnation line, $M = 8.03$.

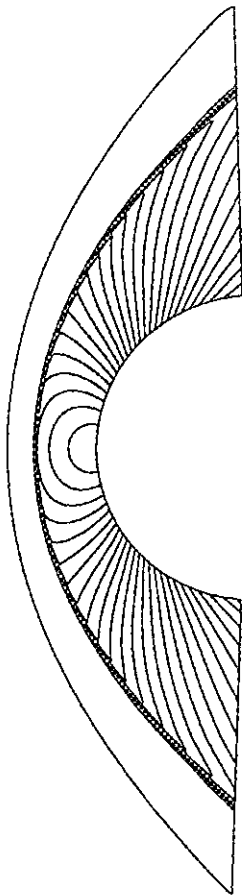


Fig. 21: Pressure contours of mean flow calculation, $M = 8.03$, coarse grid (100×80).

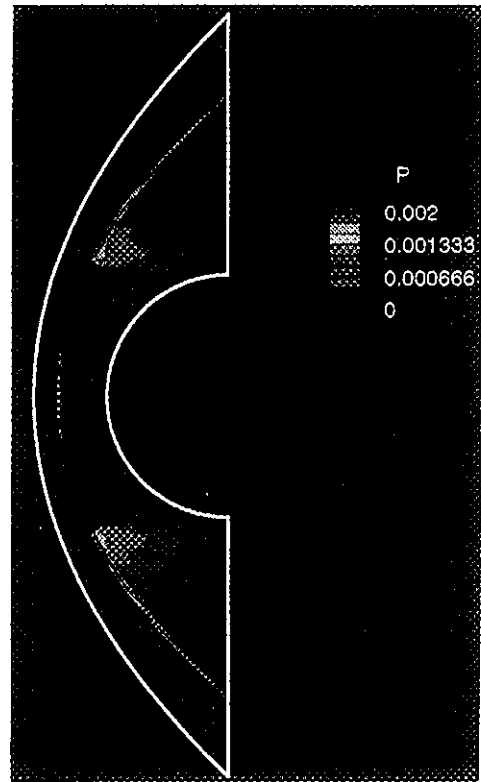


Fig. 22: Contours of pressure deviation from mean flow calculation, second-order ENO.

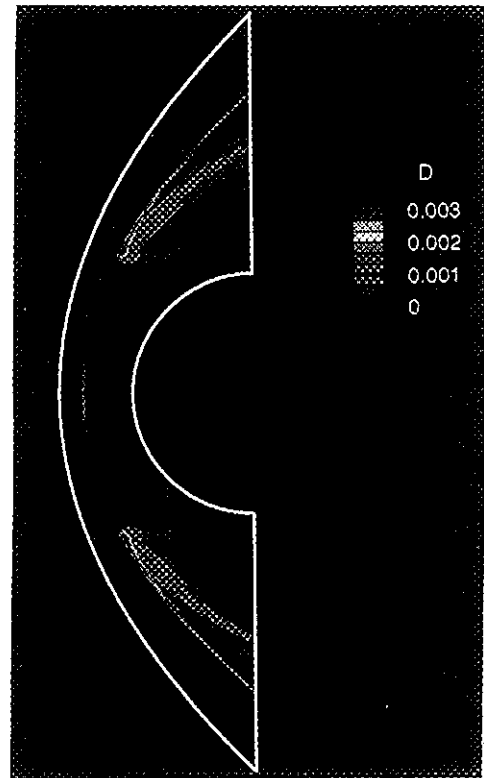


Fig. 23: Contours of density deviation from mean flow calculation, second-order ENO.

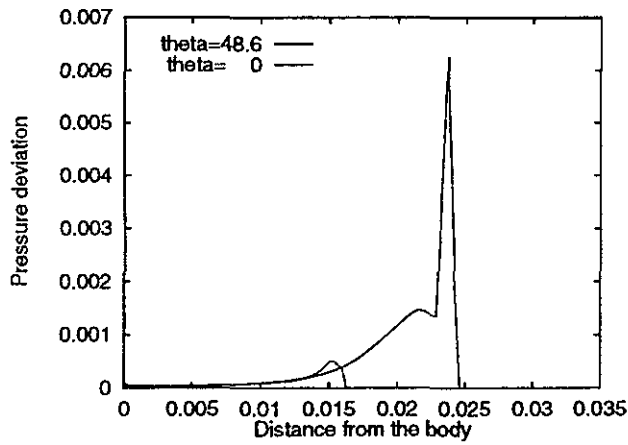


Fig. 24: Pressure deviation along $\theta = 48.6^\circ$ and $\theta = 0^\circ$ lines.

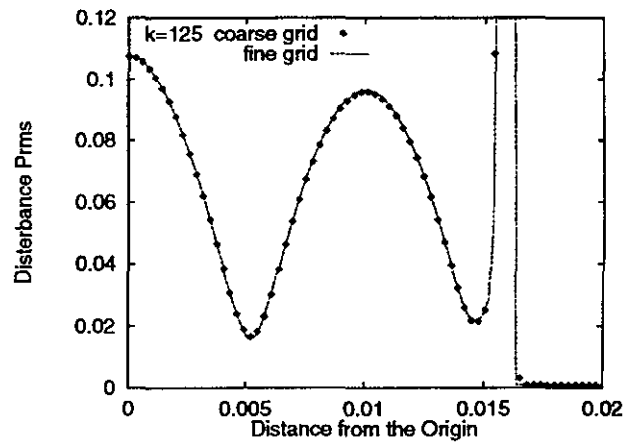


Fig. 27: Grid refinement study for root-mean-square disturbance pressure calculation, $k = 125 \text{ m}^{-1}$.

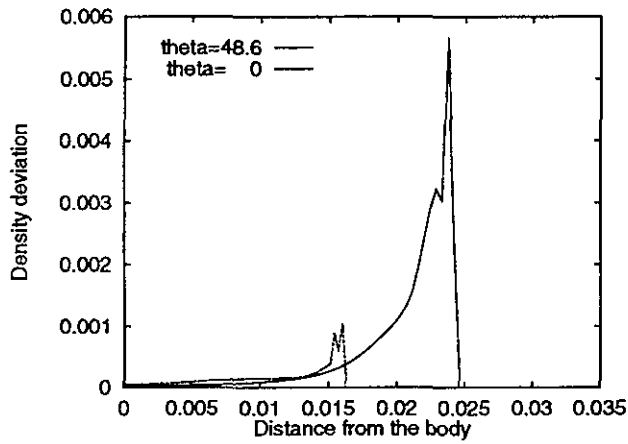


Fig. 25: Density deviation along $\theta = 48.6^\circ$ and $\theta = 0^\circ$ lines.

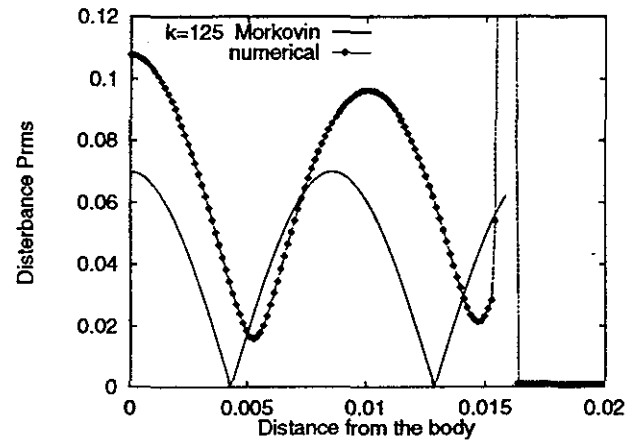


Fig. 28: Distribution of root-mean-square disturbance pressure along the stagnation line, $k = 125 \text{ m}^{-1}$.

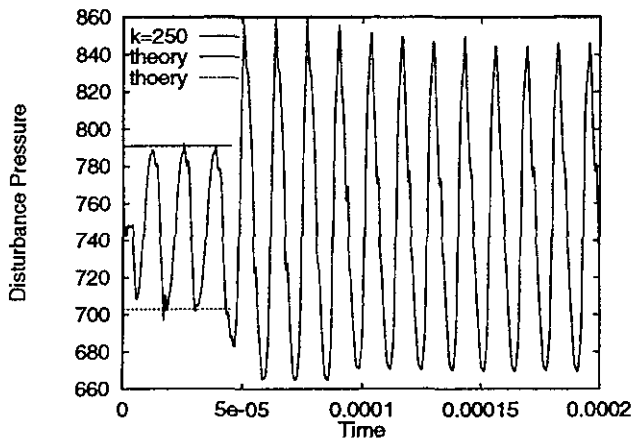


Fig. 26: Time history of instantaneous pressure behind the shock, $M = 8.03$, $k = 250 \text{ m}^{-1}$.

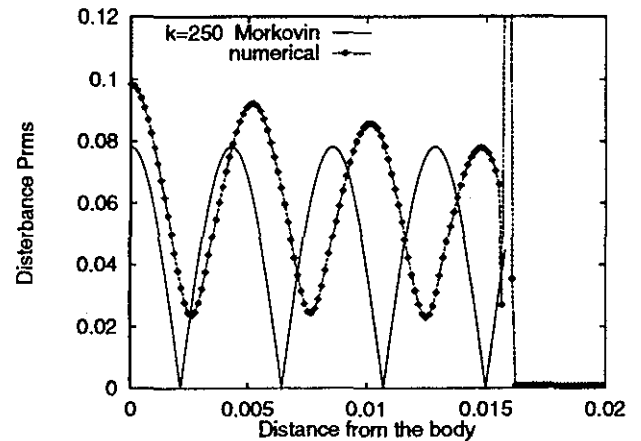


Fig. 29: Distribution of root-mean-square disturbance pressure along the stagnation line, $k = 250 \text{ m}^{-1}$.

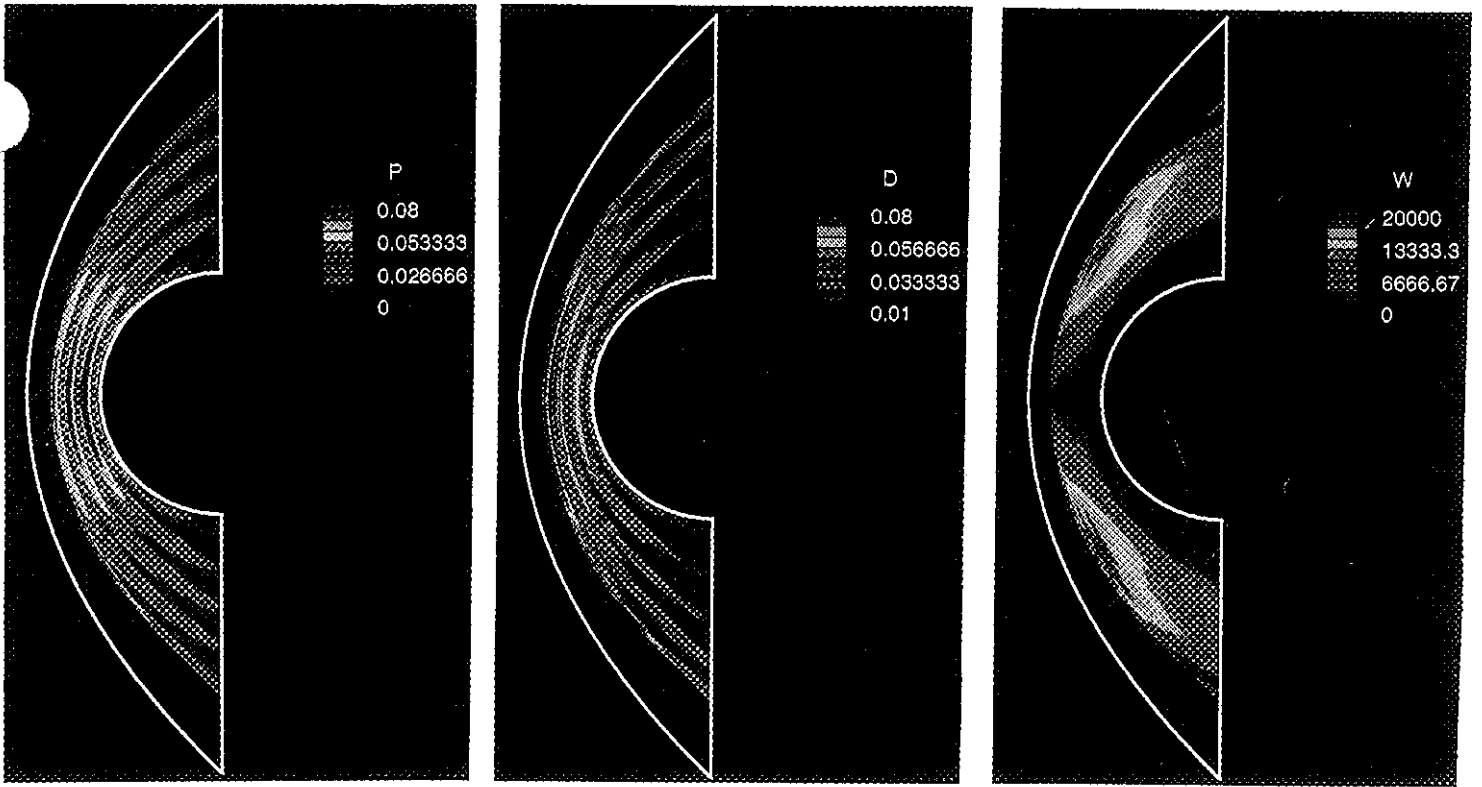


Fig. 30: Contours of root-mean-sqaure disturbance (a) pressure, (b) density, and (c) vorticity, $k = 250 \text{ m}^{-1}$.

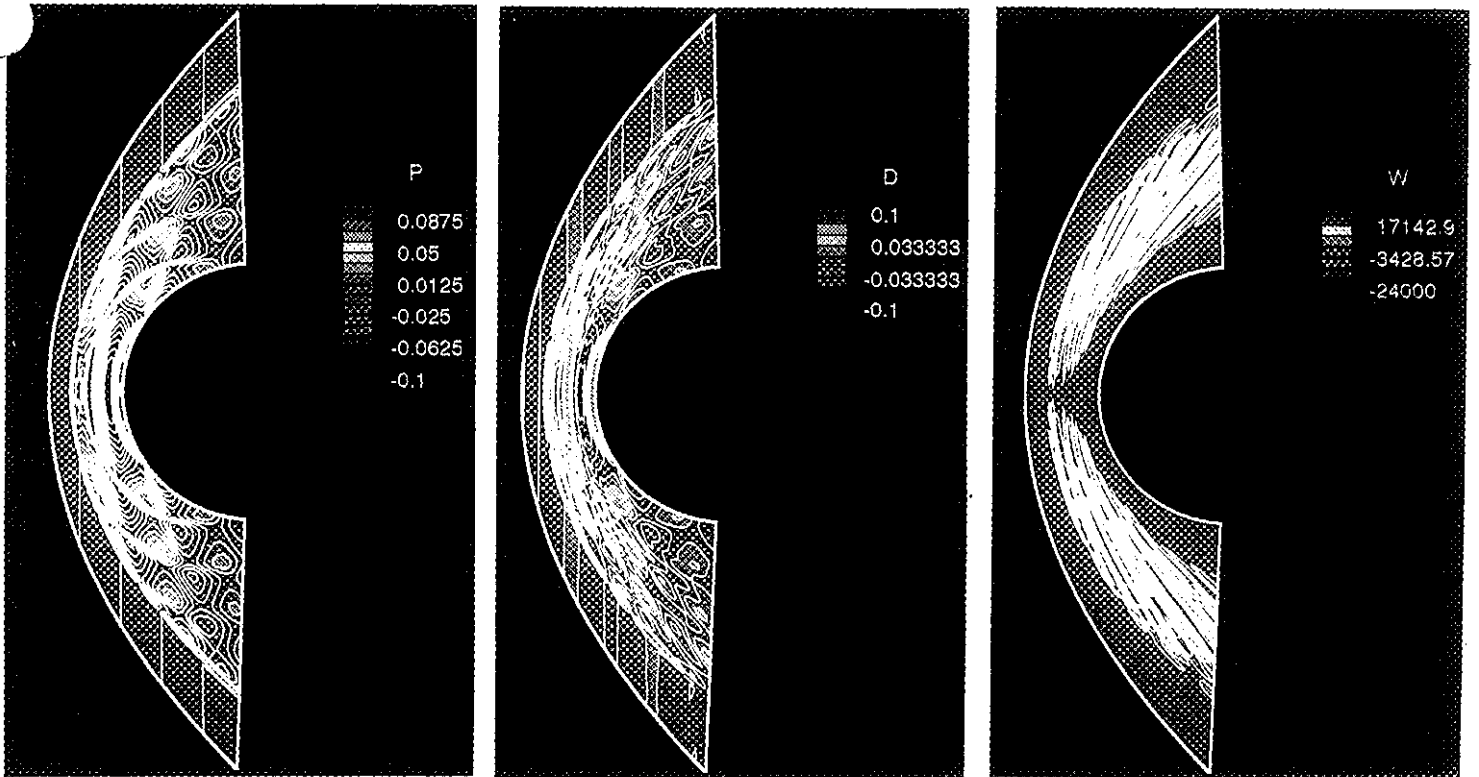


Fig. 31: Contours of instantaneous disturbance (a) pressure, (b) density, and (c) vorticity, $k = 250 \text{ m}^{-1}$.